



# Fiber-Optics-Based Aeroelastic Shape Sensing

Maxim Freydin,<sup>\*</sup> Miko Keren Rattner,<sup>†</sup> and Daniella E. Raveh<sup>‡</sup>  
*Technion—Israel Institute of Technology, 3200000 Haifa, Israel*

Iddo Kressel<sup>§</sup>

*Israel Aircraft Industry, 70100 Tel-Aviv, Israel*

and

Roy Davidi<sup>||</sup> and Moshe Tur<sup>\*\*</sup>

*Tel-Aviv University, 6997801 Ramat Aviv, Israel*

DOI: 10.2514/1.J057944

This paper presents a numerical and experimental wind tunnel study of aeroelastic shape sensing using fiber-optic sensors. Strain measurements via both discrete and distributed dynamic fiber-optic sensing technologies were used to estimate a wing's deformed shape and modal displacements using a strain-to-displacement transformation algorithm. The performance of the fiber-optic sensors and the algorithm were tested in a set of validation tests, in which the displacement response to static loads and to initial conditions was recovered and compared with that from a reference motion tracking cameras system. Excellent match of the responses validated the capabilities of the sensing configuration. The wing was tested in the wind tunnel in static conditions as well as in dynamic conditions close to and at flutter. Fiber-optics strains data were used to recover the deformed shape at static conditions, which was compared with that from aeroelastic analysis. At flutter, strain data were used to compute the wing's dynamic response and extract the flutter speed, frequency, and complex flutter mode. These were compared with aeroelastic flutter analysis and were found to be in good agreement. Overall, the study has experimentally demonstrated that strain-based aeroelastic shape sensing, both static and dynamic, is feasible and provides accurate deformations and modal responses even when based on sparse strain measurements, and when the modes used for the strain-to-displacement transformation are not the exact eigenmodes of the aeroelastic system.

## Nomenclature

$[A]$	=	transformation matrix
$g$	=	damping
$\{u\}$	=	displacement vector
$V$	=	airspeed
$\{\epsilon\}$	=	strain vector
$[\Phi]$	=	displacement modes matrix
$[\Psi]$	=	strain modes matrix
$\omega$	=	frequency
$\{\xi\}$	=	modal displacement vectors

## I. Introduction

IN RECENT years, flight vehicles are becoming progressively more elastic and, as a result, aeroelastic phenomena are becoming more prominent. A gusty environment or a high-load maneuver can result in considerable static or dynamic aeroelastic response, which, without proper control, might lead to excessive loads or even failure [1]. Hence, there is a great incentive to sense, quantify, and control aeroelastic responses. The current study focuses on aeroelastic *shape sensing*. Static shape sensing can be used to monitor the elastically deformed shape of a vehicle in trimmed flight, while dynamic shape sensing can be used to identify the aeroelastic system (frequencies

and damping) under the aircraft's operational conditions [2,3] and control it [4,5].

Shape sensing of various types of structures has been successfully demonstrated using cameras and image processing in several non-aerospace applications [6]. Model identification of simple structures in a controlled environment was also shown using high-speed video technologies [7]. In aerospace systems, the most common means for structural response measurements are accelerometers, locally attached to a few points on the structure [8]. For innovative aeroelastic configurations and applications, there is a need for alternative shape-sensing technologies that are accurate, spatially continuous, and real-time for measurement of elastic deformations. One such emerging technology is fiber-optic sensing, whose application to strain measurements is nowadays quite mature, reliable, and commercially available [9,10].

Over the past several years, fiber-optic strain sensing has seen an increased acceptance, as well as widespread use in the fields of civil engineering, aerospace, marine, and oil and gas. A prominent use of fiber-optic sensors (FOS) in the aerospace industry is for structural health monitoring of complex aerostructures [11,12]. Their inherent capabilities, including strain accuracy comparable with that of standard electrical strain gauges [13], less than 1 cm of spatial resolution, high sensitivity and wide strain dynamic range, high speed (kHz for point sensing and tens to hundreds of Hz for distributed sensing), multiplexed operation (one fiber can support many sensors), insensitivity to electromagnetic radiation, small size and light weight, as well as their suitability to be embedded into composite aerostructures without affecting their performance [14], make FOS highly suitable for aerospace systems. The ability to tailor many sensors onto a single fiber, together with their high dynamic range, makes such a sensing concept very attractive for aeroelastic applications.

FOS provide local strain measurements that need to be translated to structural deformation, for shape sensing. A review of methods to use strain data for shape sensing was recently presented by Gherlone et al. [15]. Ko et al. [16] proposed an algorithm to transform strains to displacements that is based on the relation between beam curvature and strains for a beam under bending load. The Ko displacement theory was used for deformed shape prediction on the Ikhana wing [16]. This method uses integration of strains over a straight line,

Presented as Paper 2018-0190 at the AIAA Structures, Structural Dynamics and Materials, Kissimmee, FL, 8–12 January 2018; received 20 September 2018; revision received 10 July 2019; accepted for publication 22 August 2019; published online 27 September 2019. Copyright © 2019 by Freydin, Keren Rattner, Raveh, Kressel, Davidi, and Tur. Published by the American Institute of Aeronautics and Astronautics, Inc., with permission. All requests for copying and permission to reprint should be submitted to CCC at www.copyright.com; employ the eISSN 1533-385X to initiate your request. See also AIAA Rights and Permissions www.aiaa.org/randp.

<sup>\*</sup>Undergraduate Student, Faculty of Aerospace Engineering. Student Member AIAA.

<sup>†</sup>Undergraduate Student, Faculty of Aerospace Engineering.

<sup>‡</sup>Associate Professor, Faculty of Aerospace Engineering. Associate Fellow AIAA.

<sup>§</sup>Engineering Division.

<sup>||</sup>Graduate Student, School of Electrical Engineering.

<sup>\*\*</sup>Professor, School of Electrical Engineering.

thus introducing spatial resolution errors and limits its use for beam structures. Pak [17] suggested a two-step method, in which the strains over a line are first integrated to obtain deflections and then information on the finite-element (FE) computed modes is used to map the deflections to the entire structure. Pak and Truax [18] then extended the method to predict unsteady displacements, velocities, and accelerations from strain data of an aeroelastic system (and also unsteady aerodynamic forces, in [19]). In aeroelastic applications, the aeroelastic system's properties (frequencies, damping values, and mode shapes) vary with flight conditions and as a result of changes in the system's dynamic properties (e.g., with fuel consumption). Hence, the exact aeroelastic modal characteristics are not available for mapping the deflection over the entire structure. To overcome this problem, the approach proposed by Pak [19] was to represent the aeroelastic displacements as a sum of responses of stable two-degree-of-freedom (2-DOF) dynamic systems. The frequencies and damping values were computed from an estimated ARMA model, and the coefficients were fitted using a least square technique. The method was demonstrated using simulated strains of an aeroelastic wing mode. This modeling approach might have limitations when applied to experimental data. For example, ARMA model might not yield good prediction of the damping in the system; using time histories from different sensors to generate an ARMA model does not result in the exact same modal properties; and, close to flutter, the ARMA model might only be able to capture the lightly damped mode (as the others might not be observable in the data) [3].

Foss and Haugse [20] proposed a modal approach for strain-to-displacement (STD) transformation, and Kang et al. [21] applied it experimentally for computing the dynamic structural displacements of a beam from FOS measurements. Jiang et al. [22] used the STD transformation method to estimate structural mode shapes of a cantilevered beam from fiber optics strain measurements, and Skafte et al. [23] used the method to estimate structural mode shapes of a bridge model from strain measurements collected experimentally in response to random loading. In an aeronautical application, Suh et al. [24] proposed an active flutter suppression controller based on deformations control, in which the deformations are estimated from FOS measurements, using the same STD algorithm. Suh et al.'s study was computational, with simulated strains.

The current study proposes a generalization of the STD transformation by Foss and Haugse [20] to aeroelastic shape sensing of a flexible wing, in which the modal characteristics are not known exactly. The method is demonstrated experimentally in a wind tunnel aeroelastic test. The study presents the use of the method in static aeroelastic conditions, when the deformations are fixed, as well as under dynamic conditions, when the wing vibrates close to and at the flutter onset. The study focuses on practical issues of the method implementation, such as the selection of modes for accurate deformation prediction, and comparison of static and dynamic experimental results to those from aeroelastic analyses.

## II. Strain-to-Displacement Transformation

Following Foss and Haugse [20], displacement and strain mode shapes are used to transform strain measurements to displacements as follows. We assume that the structural displacements in the physical DOF,  $\{u\}$ , can be written as a combination of displacement modes of the structure as

$$\{u\} = [\Phi]\{\xi\} \quad (1)$$

where  $[\Phi]$  is the modes matrix, and  $\{\xi\}$  are the modal displacements. Considering only the axial strain readings along the spar of a wing, the strains can be written as

$$\{\epsilon\} = \frac{\partial u}{\partial x} = \frac{\partial}{\partial x}[\Phi]\{\xi\} = [\Psi]\{\xi\} \quad (2)$$

where  $[\Psi]$  is the matrix of strain modes,  $[\Psi] = (\partial[\Phi]/\partial x)$ . The modal displacements can be computed from measured strains by least squares as

$$\{\xi\} = [[\Psi]^T[\Psi]]^{-1}[\Psi]^T\{\epsilon\} \quad (3)$$

and back substituted into Eq. (1) for a relation between the displacements and strains (the STD transformation)

$$\{u\} = [\Phi][[\Psi]^T[\Psi]]^{-1}[\Psi]^T\{\epsilon\} \quad (4)$$

When the displacement and strain modes are computed from an exact FE model of the structure, Eq. (4) should yield an accurate estimation of the displacements provided that sufficient modes are accounted for and that sufficient strain data are available for the least-squares fit [Eq. (4)]. In an experimental setup, the mode shapes used for STD transformation are likely somewhat different from those of the tested structure, even if they are based on a calibrated FE model. In aeroelastic problems the modal parameters of the structure (mode shapes, frequencies, and damping values) vary with flight conditions and we can no longer assume that the mode shapes are perfectly known at all times. In the following we argue that the STD transformation can be accurately computed based on a set of mode shapes that are comparison functions and not necessarily the eigenfunctions of the aeroelastic system. For example, for an aeroelastic system, the comparison functions can be the structural modes in vacuum. We assume that the experimental aeroelastic mode shapes can be approximated as a combination of the structural FE modes, as

$$[\Phi]_{\text{exp}} = [\Phi][A] \quad (5)$$

where the  $i$ th column of matrix  $[A]$  is the combination of the FE modes that yields the  $i$ th experimental mode. Equations (1) and (2) then become

$$\{u\} = [\Phi]_{\text{exp}}\{\xi\} = [\Phi][A]\{\xi\} \quad (6)$$

$$\{\epsilon\} = \frac{\partial u}{\partial x} = \frac{\partial}{\partial x}[\Phi][A]\{\xi\} = [\Psi][A]\{\xi\} \quad (7)$$

The modal displacements can be computed from strains by least squares as:

$$\{\xi\} = [[A]^T[\Psi]^T[\Psi][A]]^{-1}[A]^T[\Psi]^T\{\epsilon\} \quad (8)$$

Back substitution into Eq. (6), and using the fact that  $[A]$  is a square matrix, we end up with Eq. (4). This implies that the mode shapes used in the STD [Eqs. (3) and (4)] do not have to be the eigenfunctions of the tested structure. Modes of a similar model, for example, those of an approximate FE model, can be used as comparison functions, as long as the exact modes can be represented as a linear combination of them. This is similar to the local correspondence principle described by Brincker et al. [25]. Also, Pak and Truax [18] demonstrated the two-step method on two versions of a wing model, using the eigenfunctions of one as comparison functions for the other in the two-step method approach, and noted that by doing this "the quality of the results are not degraded too much."

## III. Test Case: An Elastic Wing Model

Fiber-optic aeroelastic shape sensing, based on the STD transformation, was studied numerically and experimentally on an elastic wing model. The wing was designed to be flexible and to experience flutter within the speed range of the wind tunnel. Geometrically, it was designed considering the wind tunnel facility constraints. The chamber at the Technion's subsonic wind tunnel has a rectangular cross section of 1 m<sup>2</sup> and a maximum airspeed of 100 m/s. Based on these constraints, a 0.1-m-chord, 0.6-m-span rectangular wing was designed, with a NACA0018 airfoil. The corresponding Reynolds number at 50 m/s is  $3.4 \cdot 10^5$ .

Figure 1a shows the wing CAD model including the base with which the wing attaches to the wind tunnel floor. The wing structure is made of two rectangular cross-sectioned spars with dimensions of 18 mm  $\times$  5 mm and 11 mm  $\times$  5 mm for the front and rear spars,

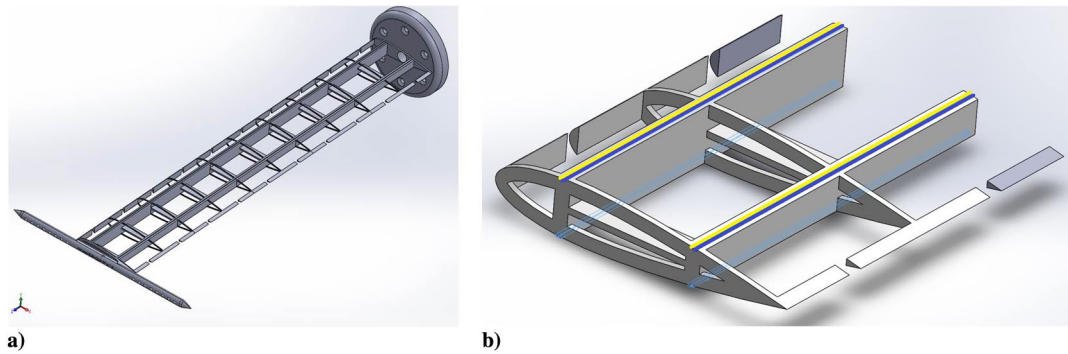


Fig. 1 a) Wing CAD model and b) optical fibers (in yellow and blue) on a segment of the wing CAD model.

respectively. Thin plates connect the two spars for additional bending and torsional stiffness. A laminate film is wrapped around very thin ribs and small leading and trailing edge parts (nonstructural elements) to provide the external wing shape, as well as additional torsional stiffness. The wing structure weighs 170 g. At the wing tip, a rod of 10 mm diameter extends in front of the leading edge and behind the trailing edge. A concentrated weight can be attached to this rod in order to alter the wing's inertial properties, and consequently the wing's natural frequencies, modes, and flutter dynamic pressure.

The wing structure was printed in rapid prototyping, using ULTEM-9085 (<http://www.stratasys.com/materials/fdm/ultem-9085>). The printed material elasticity modulus was verified in a tensile test. For the following FE analyses, a value of 2500 MPa was used. The wing was covered by a 12  $\mu\text{m}$  Oraclear iron-on laminate film that is used for radio-controlled drones (<https://www.oracover.de>). The film's elasticity modulus was estimated as 1050 MPa.

#### A. Fiber-Optic Sensing Network

Fiber Bragg grating techniques can provide discrete point or distributed sensing [26–28]. With the goal of performing shape sensing, we have harnessed two types of fiber optic sensors [26]: 1) *Discrete fiber Bragg gratings (FBG)* [27], in which a few FBGs of different strain-sensitive wavelengths of peak reflection are imprinted on a single strand of fiber. For interrogation we used the four-channel Micron-Optics sm130 (<https://www.MicronOptics.com>), capable of covering a wide strain dynamic range of several thousands of microstrains with sampling rates up to 2500 Hz; 2) *Continuous fiber Bragg grating (CFBG)* [28], comprising a tight concatenation of FBGs, all initially of the same wavelength of peak reflection, individually imprinted along the whole length of the fiber. Because the wavelengths of peak reflection of these FBGs may not be distinct, proper interrogation is more challenging and coherent techniques must be employed. The interrogator used in the current experiment was the Sensuron RTS125+ (<https://www.sensuron.com/rts125/>). It has eight channels connecting the instrument to eight so-called broadband reflectors, each feeding one  $\leq 13$  m CFBG fiber through a few meters of a standard single mode fiber. With a spatial spacing of 6.33 mm, 1 m of a CFBG fiber allows for the distributed sensing of strain at more than 150 independent points. In the current implementation of this sensing methodology, the sampling rate must be traded off against the available strain dynamic range: Although a dynamic range of more than 10,000  $\mu\text{s}$  is possible at a sampling rate of a few tens of Hz, it shrinks to a window of less than 2000  $\mu\text{s}$  if the maximum available sampling rate of 100 Hz is used. Both interrogation techniques offer strain sensitivities of a few microstrains.

##### 1. Fibers Layout

The sensing fibers were embedded in 2 mm  $\times$  0.5 mm channels printed in the spars on both sides of the wing (see Fig. 1b) and attached with epoxy. Four polyimide-coated fibers, each with nine discrete 4-mm-long FBGs, were installed on the two sides of the two spars. Two ORMOCER-coated CFBG fibers were attached to the spars sharing the same dedicated channels as the discrete FBG fibers. However, unlike their discrete counterparts, each CFBG fiber run

over the front spar, from the wing root to the tip, and continuously back along the rear spar. Overall, on each side of the two spars, strain data were measured via 9 discrete FBGs and 95 CFBGs. Figure 2 shows the wing with embedded optical fibers. The sensing optical fibers are connected to their respective interrogators through holes in the wing base and the tunnel floor.

##### 2. Locations of the Sensing Points

1) *Discrete FBGs*: Harnessing the sensitivity of FBGs to heat, their locations were determined to within 2 mm by a careful uniform scanning of each of the four channels with a transverse thin hot wire, looking for the spatial coordinates that maximize the change in the recorded wavelength. Four channels of the Micron-Optics sm130 were used to monitor the four discrete FBG fibers.

2) *CFBGs*: Because of the layout of the CFBGs, two instrument channels had to be monitored. The Sensuron interrogator starts counting the resolution cells along the fiber from the beginning of the CFBG fiber. To establish a one-to-one correspondence between the instrument reading and the actual physical location of a particular resolution cell on a spar, the locations of ribs 3, 5, and 7 (counting from the base) were identified using the same heating technique. This procedure leaves an uncertainty of one sensor length, that is, 6.33 mm.

#### B. Motion Recovery Cameras System

To evaluate the accuracy of the FOS systems, wing deformations were captured in a static loading experiment by an OptiTrack (<http://optitrack.com>) Motion Recovery System (MRS). The latter consists of a 12 *Prime 13* cameras array mounted on a truss rig that tracks the locations of passive reflectors in space. The system was configured to give the 3-DOF location of 12 reflectors at a rate of 135 Hz in a sub-millimeter accuracy. Figure 2a shows the wing with the attached 12 reflectors: 10 along its leading and trailing edges and 2 on the front and rear tips of the wing-tip bar.

#### C. Finite-Element Model and Modal Analysis

MSC Nastran (<http://www.mscsoftware.com/product/msc-nastran>) FE model was constructed from the CAD model. The spars, connecting bars, and skin were modeled using plate elements and the rod at the wing tip was modeled using rod elements (Fig. 3a). The leading and trailing edge elements were modeled as concentrated masses. The wing model is clamped at the root. The FE model has about 9000 grid points, 8500 plate elements, and 500 beam elements.

Massless rod elements with negligible stiffness were attached to nodes along the front and rear spars. These elements do not contribute to the stiffness or inertial properties of the model. They are there to provide information on the strains at their locations. The nodes of these elements are placed at the geometrical locations of the FOS (which vary between the FBG and CFBG fiber systems). In this way, these rod elements serve as *virtual strain gauges*, providing the computed strains at the FOS locations from the FE analyses. Figure 3b shows a schematic plot of such a rod element, connecting two nodes on the front spar.

Modal analysis provided the frequencies and mode shapes of the wing, both displacement and strain modes. Figure 4 shows the first

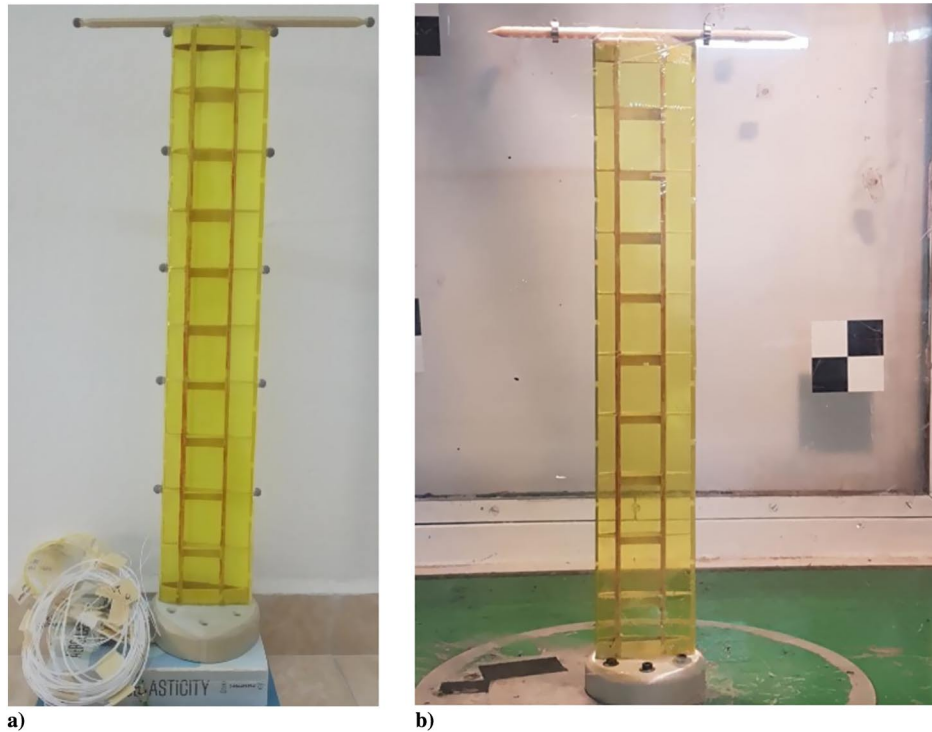


Fig. 2 a) Wing model with reflectors (used in the verification test) and b) the wing mounted in the wind tunnel.

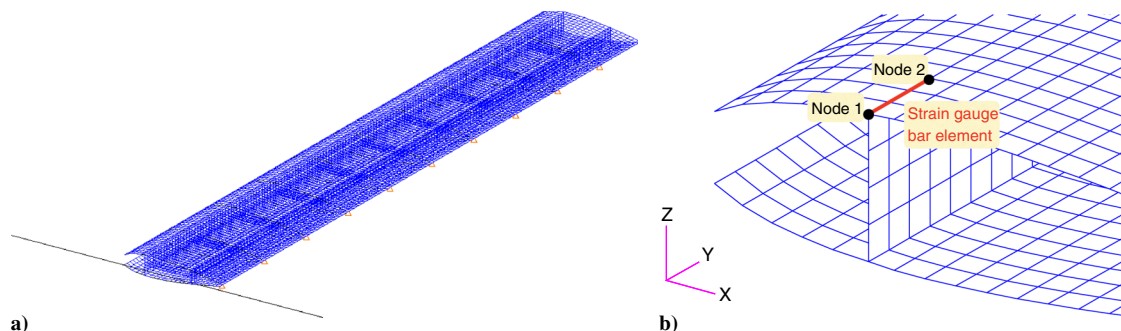


Fig. 3 a) Wing FE model and b) zoom on the front spar and skin plate elements and a schematic of a bar element that is used as a strain gauge in the FE model.

four displacement modes with their frequencies (the skin is not shown). Strain modes are also computed in the modal analysis. They are arranged as column vectors in matrix  $\Psi$  [Eq. (2)], where each column represents a single strain mode, provided in the virtual strain-gauge element nodes, which are also the FOS locations.

## IV. Results

Two sets of experiments were carried out. The first set comprised static and dynamic measurements of deformations in response to static loading and to initial deformation perturbation, respectively. These experiments were conducted outside of the wind tunnel. Shape sensing based on the FOS measurements and the STD algorithm was assessed by comparing the calculated displacements to those measured by the MRS. These tests validated the methodology and algorithm implementation for static and dynamic deformation cases.

The second set of experiments was performed at the Technion subsonic wind tunnel and included static and dynamic response cases. In the static case, wing displacements were calculated from strain measurements in flow conditions of fixed airspeed and angle of attack and compared with displacements from numerical aeroelastic analysis. Then, at a fixed angle of attack of zero degrees, the airspeed was gradually increased until flutter onset conditions were reached and an exponentially growing response was detected. Several cycles

of motion before and at flutter were recorded. The dynamic wing motion was recovered from FOS measurements using the STD algorithm and compared with the wing motion at flutter as predicted by an aeroelastic flutter analysis.

### A. Validation Tests

#### 1. Wing Deflection Under Static Loads

The system's performance was evaluated in a static test in which the wing was loaded in bending and torsion by weights. Wing deformations were computed from FOS strain measurements and compared with those captured by the MRS. In the first test, the wing was loaded by a 200 g weight at the wing tip center chord. In a second test, the wing was loaded by 200 g downward load at the wing tip, 80 mm ahead of the leading edge, and 200 g upward load at the wing tip, 80 mm behind the trailing edge, generating a torsion load.

Figures 5 and 6 show the statically deformed wing shape as computed from CFBG strains (black dots), and as captured by the MRS (red circles) for the two loading cases. Both figures show good agreement between the two deformed shapes. For the bending and torsion load cases, the maximum displacements measured by the MRS at the rear end of the wing-tip rod were  $-18.58$  mm and  $-29.11$  mm, respectively. The relative difference, according to Eq. (9), is 2.66% and 2.53%, respectively. Similar results were obtained with the FBG strain data.

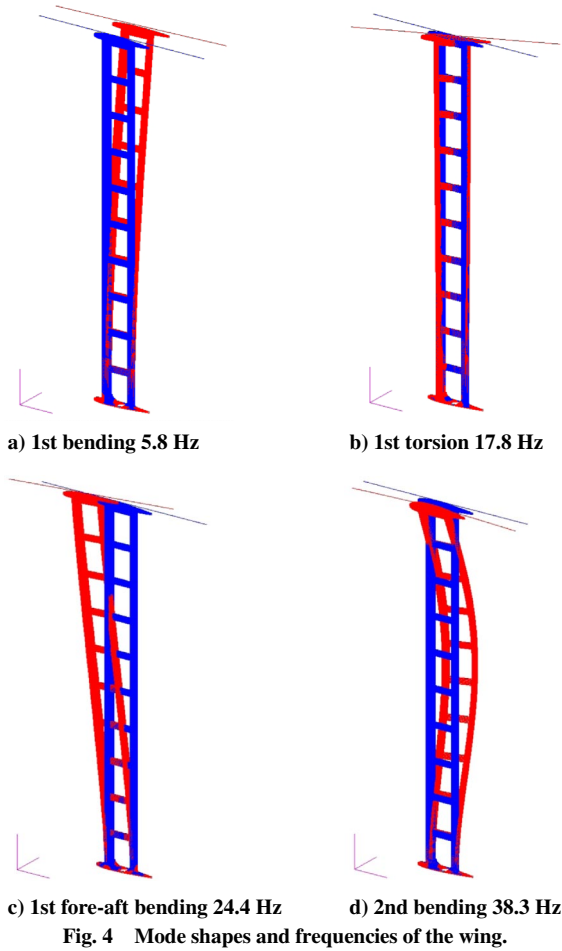


Fig. 4 Mode shapes and frequencies of the wing.

$$\Delta \bar{y} = 100 \frac{y_{MRS} - y_{STD}}{y_{MRS}} \quad (9)$$

2. Wing Dynamic Response to Initial Conditions

Time-varying deformations can be computed by applying the STD algorithm on a series of snapshots of recorded strains; that is, wing deformations are computed each time the strains are sampled and are then concatenated to provide the dynamic response. Figure 7 shows the wing-tip leading edge displacement response to initial conditions as computed from strain data and as captured by the MRS. In this test, the wing was deformed by a bending load and then released from a static position. Strains were measured by the CFBG at 100 Hz in the strain limits of  $\pm 1200 \mu s$ . Good agreement between deflections computed from strains and those captured by the MRS is demonstrated after the first 0.5 s of the response. Differences in the first cycles of the response are attributed to the strain sensor's saturation due to the too large initial deformations. From Fig. 7, the response frequency is 5.8 Hz, which corresponds to the first bending-mode frequency.

3. Considerations in Mode Selection for the STD Transformation

Implementing the method described in Sec. II for a given structure with given locations of the strain measurement nodes requires selection of the modes that will be used in matrices  $[\Phi]$  and  $[\Psi]$ . It is tempting to use as many structural modes as possible in hopes to achieve more accurate results. However, we recall that Eq. (3) solves a least squares problem for the measured strains, and therefore overfitting might occur if too many modes are fitted, or not enough measurement data are available.

Overfitting is easily tested by a two-step process. First, calculate the estimated modal displacements as described in Eq. (3) and then use them to reconstruct the strains [Eq. (2)] at all of the structural grid points using an extended  $[\Psi]$  matrix that includes the full FE strain mode shapes (not only at the strain measurement points). By plotting

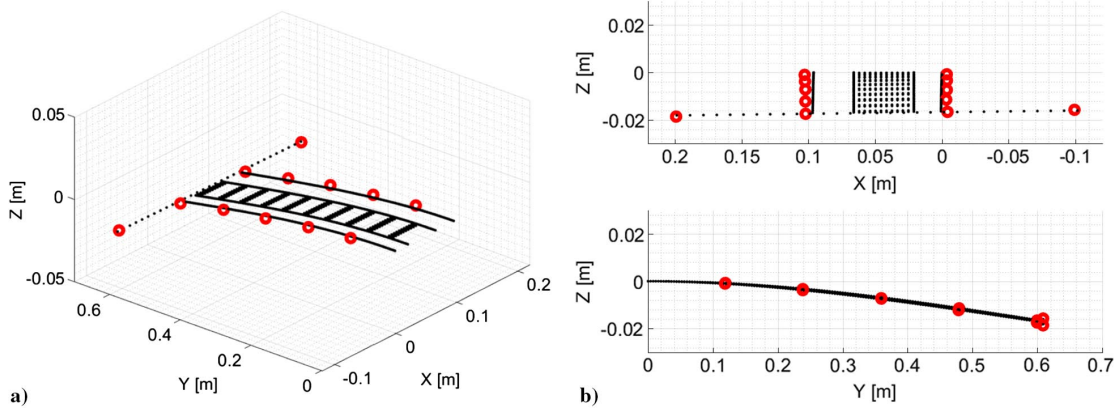


Fig. 5 Wing deflection due to static bending loading as computed from strains and captured by the MRS. a) Isometric and b) side views.

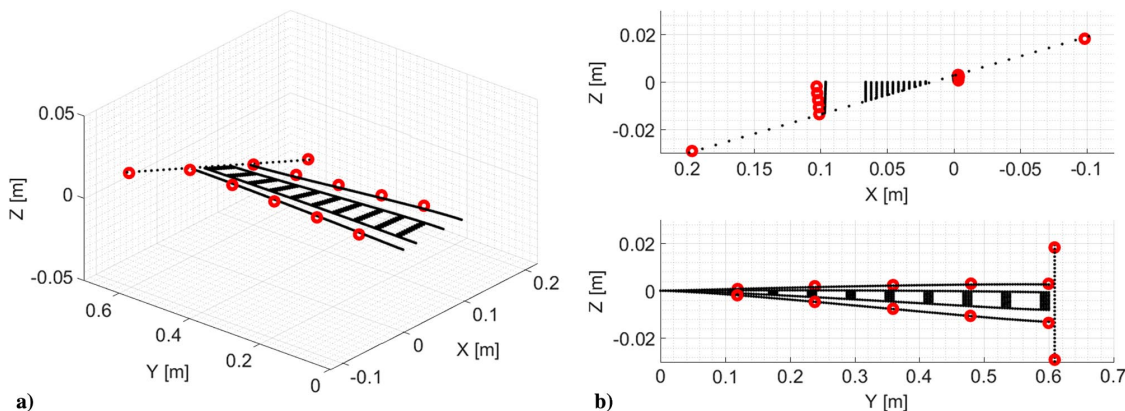


Fig. 6 Wing deflection due to static torsion loading as computed from strains and captured by the MRS. a) Isometric and b) side views.

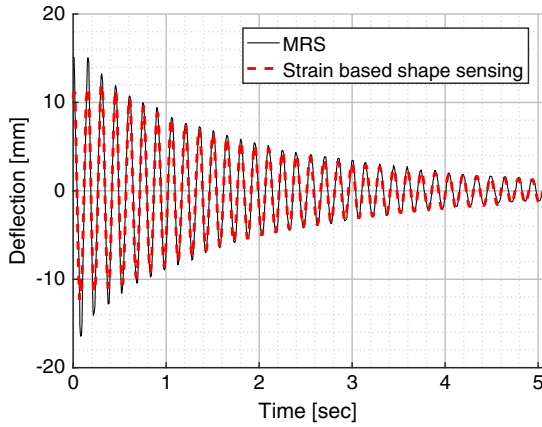


Fig. 7 Wing tip dynamic displacement, calculated from CFBG-measured strain in response to bending initial conditions.

the measured and the reconstructed strains on the same figure, overfitted strain measurements are easily identified and the number of used modes can be selected accordingly. For example, Fig. 8 shows the measured and reconstructed strains computed using the first 2, 4, 6, and 10 modes with only 5 strain measurements on each spar. It is evident that using 10 modes results in overfitting of the data. For the least-square procedure, clearly, the dense CFBG data are superior to the sparse FBG. However, in the current study there were sufficient FBG strain measurements, and the use of FBG and CFBG data resulted in similar reconstructions of strains and displacements in all of the cases.

Another consideration when constructing the STD projection matrix is the possibility that two strain modes might have similar, or close to similar, strain values at the strain measurement nodes. For example, an out-of-plane and in-plane bending modes will have similar mode shapes, varying linearly from some value at the clamped end to zero at the free wing tip (up to the strain sign for fibers on the top and bottom of the wing). Mathematically, such mode shapes are parallel. Such modes can be identified and eliminated by checking the orthogonality of the strain modes that are candidates for use in the STD transformation matrix. An orthogonality matrix  $[T]$  can be calculated as:

$$T_{ij} = \frac{\{\Psi_i\}^T \{\Psi_j\}}{\sqrt{\|\{\Psi_i\}^T \{\Psi_j\}\|}} \quad (10)$$

$T_{ij} = 1$  represents parallel modes and  $T_{ij} = 0$  represents orthogonal modes. Elements of  $[T]$  can then be plotted as a surface (see Fig. 9) and modes with  $T_{ij}$  values higher than some threshold can be eliminated. Figure 9 shows the orthogonality matrix computed for the first 10 strain modes with 5 measurement nodes on each spar.

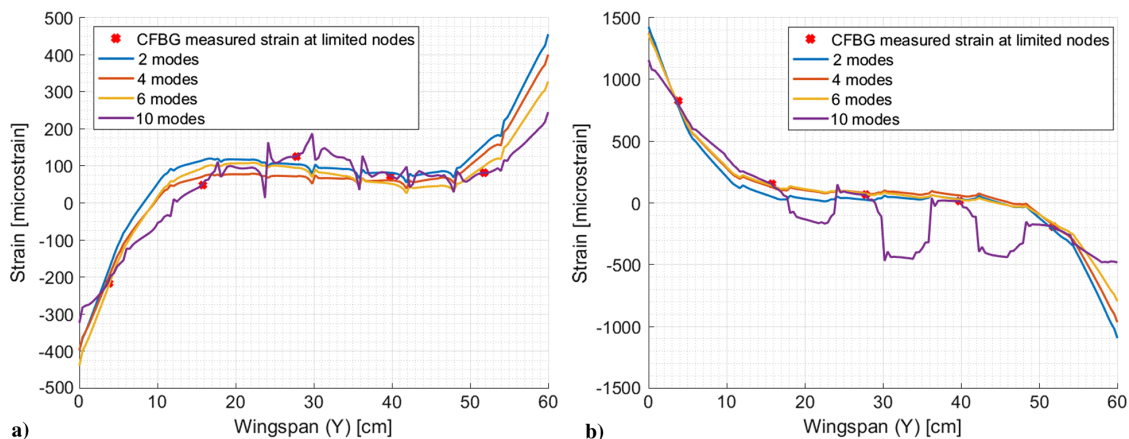


Fig. 8 Measured vs reconstructed strain based on a limited number of sensors: a) front spar; b) rear spar.

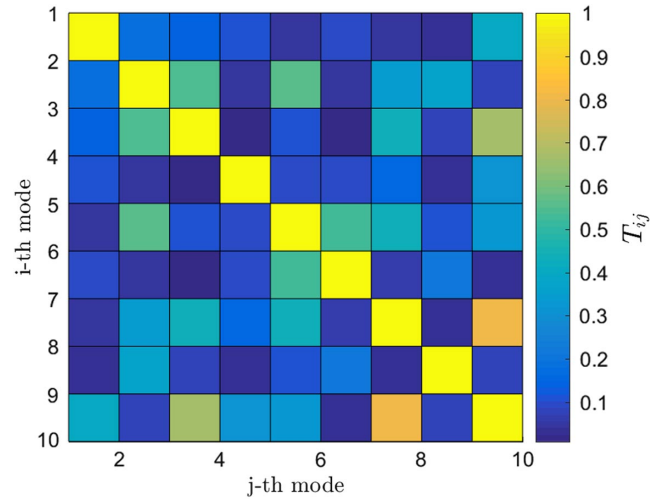


Fig. 9 Orthogonality matrix of the first 10 modes for 5 strain measurement nodes on each spar.

One last thing to keep in mind when selecting modes is the fact that some modes are unlikely to participate in a response due to the nature of the physical problem. In the current work, it is reasonable to assume that all fore-aft in-plane bending modes can be ignored when constructing the transformation matrix [see mode (c) in Fig. 4]. The wing structure is stiff in the in-plane bending direction, and the aerodynamic force acting in this direction is significantly lower than the perpendicular force. Thus, the in-plane bending should have negligible contribution to the wing's deformation. Following all guidelines listed above, five modes were used in this study, which are the first low-frequency modes, excluding the first and second in-plane bending modes.

## B. Wind Tunnel Tests

Two wind tunnel tests were performed. In the static test, the wing was installed at 5 deg angle of attack and was tested at free-stream velocity of 20 m/s, which is significantly below the flutter onset. Strain measurements were recorded in an almost static condition. In the dynamic experiment, the wing was installed at a zero angle of attack and the free-stream velocity was increased until flutter onset was detected. Strain measurements were taken during the wing's dynamic response close to flutter and at flutter.

For reference and comparison, static aeroelastic and flutter analyses were carried out with the ZAERO software (<http://www.zonatech.com/ZAERO.htm>), based on a linear panel aerodynamic model, in which the wing was divided to 9 chordwise and 17 spanwise aerodynamic panels. Figure 10 shows an  $\omega$ - $V$ - $g$  plot, presenting the variation of the aeroelastic frequencies and damping values of the first four aeroelastic modes as a function of airspeed

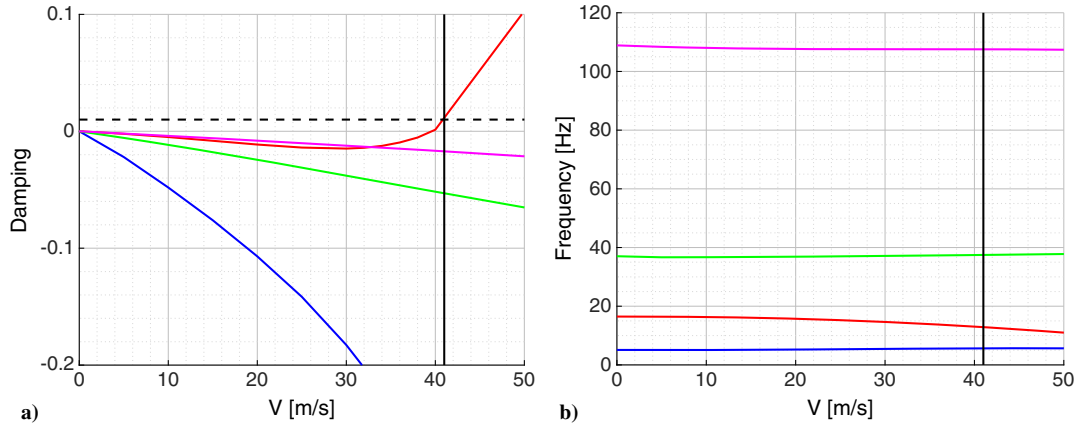


Fig. 10  $\omega$ - $V$ - $g$  plot for the wing with tip weights; the vertical line is at the computed flutter speed, based on 1% structural damping.

(not including the in-plane bending mode). Assuming a typical 1% structural damping (marked on Fig. 10a as a black dashed horizontal line), flutter is expected to occur at about 41 m/s, with a flutter frequency of about 13 Hz. The flutter analysis provided a speed range of operation to the wind tunnel test.

In the flutter test, two 10 g weights were attached to the wing tip rod, one ahead of the leading edge and one behind the trailing edge (see Fig. 2b). At flutter onset, due to the large wing vibrations, the trailing edge weight, which is not fixed to its place, separates and flies off of the wing, and consequently the flutter onset velocity increases and flutter stops. This serves as a safety mechanism to save the wing from structural failure during the test while allowing to test the wing all the way to flutter onset. Figure 10 presents flutter analysis results for the wing configuration with the added weights.

1. Static Conditions

Figure 11 shows the deformed wing shape due to static aerodynamic load at 5 deg angle of attack and 20 m/s free-stream flow velocity as predicted by the aeroelastic analysis and by the STD algorithm based on CFBG strains. Although at these conditions the wing should be static, strain fluctuations were measured due to the natural turbulence of the open-loop tunnel. Thus, the strain data were averaged over 5 s period before their usage for calculation of wing deformation.

Figure 11 presents good agreement between the theoretical and strain-based deformations of the wing. The displacement computed by the aeroelastic analysis at the wing tip at  $x = 0.2$  m (rear end of the wing-tip rod) is  $-21.28$  mm. The relative difference between the strain-based and computed deformation, according to Eq. (9), is 8.1%. This difference can be attributed to the fidelity of the FE model, especially in the torsional stiffness, which is mostly due to the laminate film. Uncertainties in material properties of the film and the quality of adhesion to the wing structure are likely to affect the wing's torsional stiffness and consequently the computational results.

2. Dynamic (Flutter) Conditions

Figure 12 shows strain-based calculated deflection of the wing tip at the leading and trailing edges when the free-stream velocity was increased to 40 m/s. The first 1.5 s of the displacement data shows a bounded, lightly damped response to the natural turbulence of the wind tunnel. At 1.5 s, the response starts to grow exponentially when the flutter onset airspeed is reached. Displacement differences between the leading and trailing edges suggest that a combined motion of twist and bending is taking place, as is common in a bending-torsion flutter mechanism.

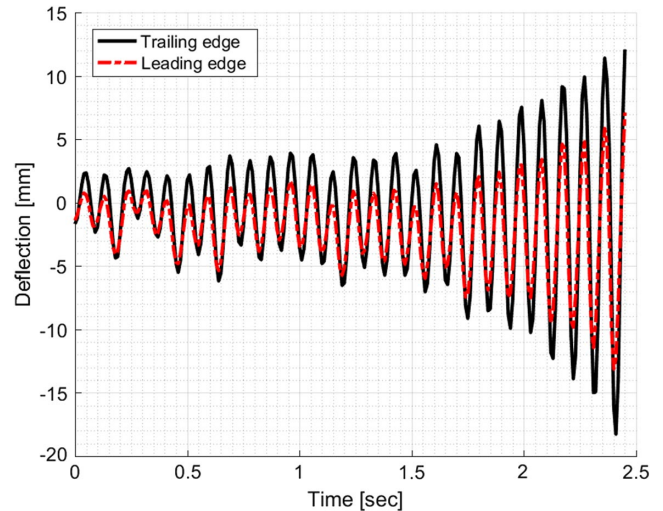


Fig. 12 Wing tip displacement time series during flutter, leading, and trailing edges.

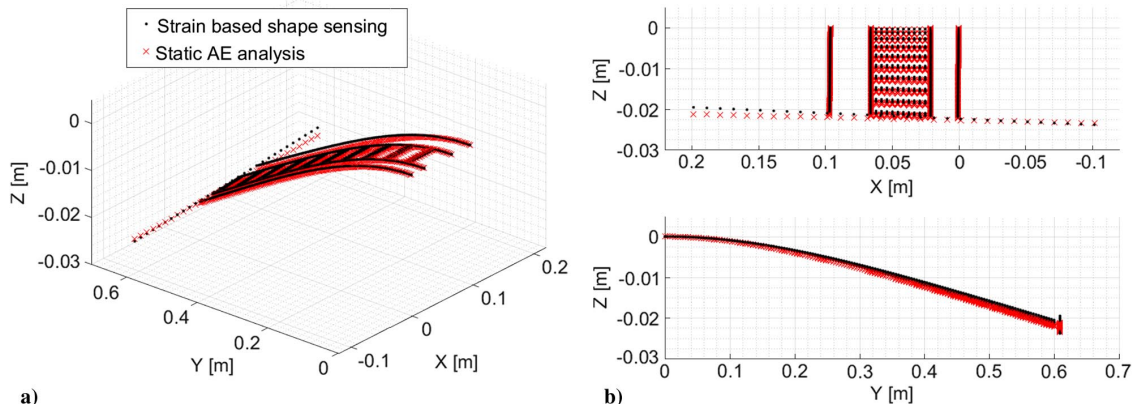


Fig. 11 Wing deflection due to static loading; 5 deg angle of attack, 20 m/s.

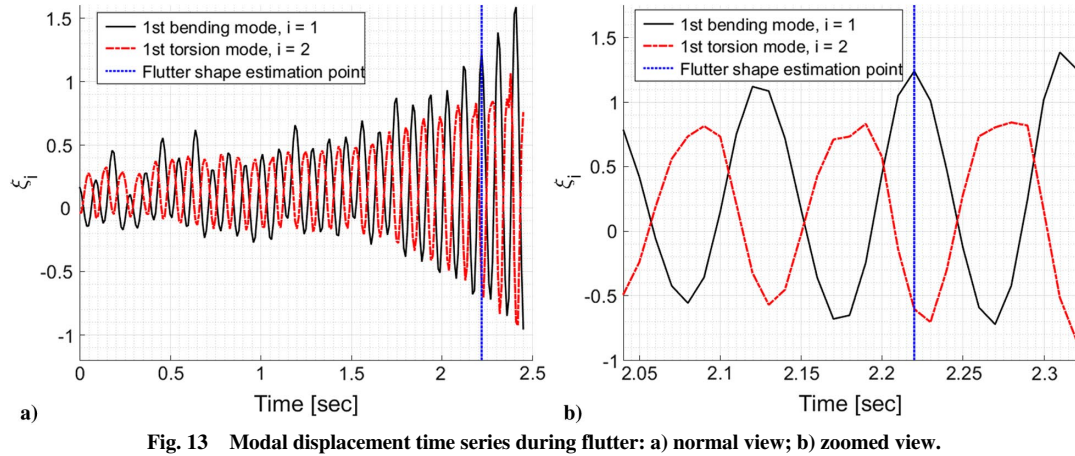


Fig. 13 Modal displacement time series during flutter: a) normal view; b) zoomed view.

Figure 13 shows the time history of the modal displacements of the first bending and torsion modes. In the first 1.5 s of the response, before flutter onset, the modes respond to the unsteadiness of the free-stream flow. As the wind tunnel's velocity increases and flutter starts, the two modal displacements grow exponentially while maintaining a constant amplitude ratio and phase between them. Figure 13b shows a close-up view at a few of the peaks in which the phase and amplitude ratio between the modes are visible and can be extracted. Figure 14 shows the modal displacement time history for higher modes. In comparison to the modal displacements of the first two modes (Fig. 13), it is evident that throughout the recorded response, higher modes contribute an order of magnitude less to the displacement.

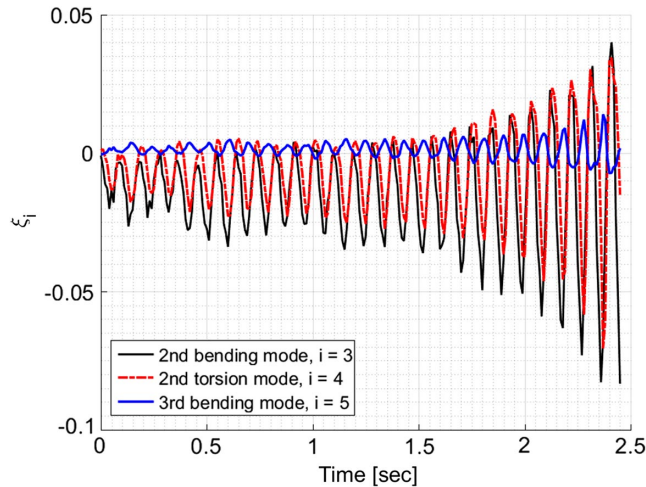


Fig. 14 Modal displacement time series during flutter for higher-order modes.

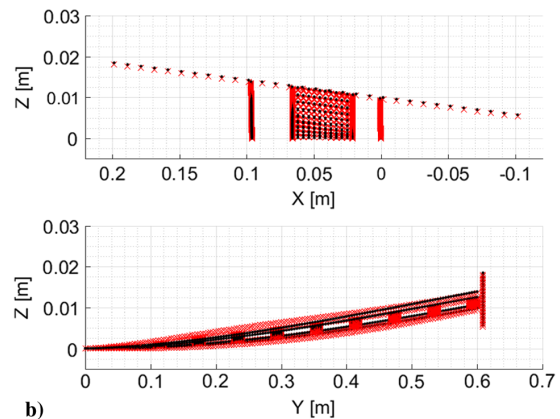
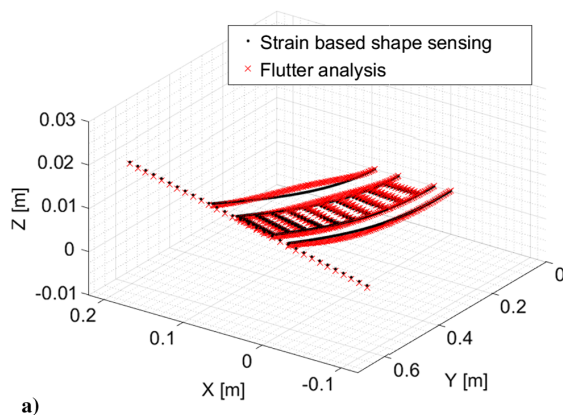


Fig. 15 Wing deflection at flutter as computed from strains and predicted by ZAERO. a) Isometric and b) side views.

However, their contribution is well identified. It is noted that all modal coordinates were normalized such that a unit of modal participation produces a maximum displacement of 10 mm along the beam. This normalization allows comparing the relative contribution of the modes to the total displacement.

Comparison of the analytical and experimental results includes the flutter onset speed, flutter frequency, and flutter mode. At the wind tunnel, diverging responses started at about 41 m/s, similar to the analytical prediction assuming 1% damping ratio. The experimental flutter frequency, as computed from Fourier analysis of the time response, is 11 Hz, compared with 12.9 in the ZAERO analysis. As in the static case, errors can be contributed to the model fidelity and to measurements.

The wing's motion at flutter can be expressed as

$$\{u\} = [\Phi]\{\xi_f\}e^{i\omega_f t} \quad (11)$$

where  $\{\xi_f\}$  is the complex flutter mode that includes the amplitude ratio and phase angles between the modal displacements at flutter. The flutter mode was estimated from the modal time histories in Fig. 13 at the time of flutter onset, which is indicated by the vertical dashed blue line. Figure 15 shows a very good agreement between the experimental and numerically computed flutter mode shape. The phase lag between the bending and torsion modes is 152 deg from the experimental data, and 169 deg from the analysis. The clear and accurate identification of the modal motion at flutter and at lower velocities can be used for control of the wing's dynamic response to atmospheric turbulence and flutter suppression.

## V. Conclusions

This paper presented a wind tunnel study of aeroelastic static and dynamic shape sensing using a fiber-optic sensing network with a negligible effect on the mechanical and other properties of the wing. Physical and modal deformations were computed based on

measured strains and the strain-to-displacement (STD) transformation algorithm, which uses deformation and strain mode shapes from a finite-element model. The methodology was tested in a dedicated wind tunnel test of an elastic wing, in which strain measurements over the wing spars were recorded using two fiber-optic technologies, the *fiber Bragg gratings (FBG)* and *Continuous fiber Bragg grating (CFBG)*.

A set of validation tests was conducted, in which the wing's static response to fixed bending and torsion loads and the wing's dynamic response to initial conditions were computed from strain data and compared with those from a reference motion recovery cameras system. Very good match of the displacements validated the use of fiber-optic sensors (FOS) and the STD algorithm for static and dynamic shape sensing. The results were used to explore the sensitivity of the resulting deformations to the amount of strain data and to the selection of modes that are used in the STD transformation. For the current test case, both the FBG and CFBG provided sufficient data for accurate recovery of the displacements. The paper suggests some guidelines for appropriate selection of modes.

The wing was then tested in the wind tunnel at static conditions of fixed angle of attack and airspeed, and then in increasing airspeeds, all the way to flutter. Wing deformation at the static conditions were computed based on the strain data and compared with results from ZAERO static aeroelastic analysis. For the dynamic case, snapshots of recorded strain data were used to recover the wing's deformation and modal response at airspeeds close to flutter and at flutter. The flutter onset speed, flutter frequency, and flutter mode shape were extracted and were shown to be in good agreement with the computational ones.

It was shown experimentally that strain-based aeroelastic shape sensing, both static and dynamic, is feasible and provides accurate deformations and modal responses even when based on sparse strain measurements (in all cases there was no significant difference between results from the FBG and CFBG FOS). It requires prior knowledge of the modal model, including displacements and strain modes. However, it was shown that the model does not have to be exact, and for aeroelastic applications the structural (in vacuum) modes of a coarse dynamic finite-element model can be used successfully.

Compared with accelerometers and strain gauges, which are typically used to measure structural responses in flight, FOS are light weight, are sensitive, and offer high spatial resolution measurement. They can be conveniently embedded in composite-material wing structures (without compromising the structure strength), and due to their inherent multiplexing capabilities they do not require cabling for each sensor. The use of FOS for aeroelastic shape sensing may provide means to sense and control the static wing shape in trimmed flight, predict, detect, and control flutter, and sense and control the dynamic response due to gust and other dynamic loading cases. Finally, it is noted that all the wing models and the data from the wind tunnel experiment are available at <https://a3tb.net.technion.ac.il/>.

## References

- [1] Noll, T. E., Brown, J. M., Perez-Davis, M. E., Ishmael, S. D., Tiffany, G. C., and Gaier, M., "Investigation of the Helios Prototype Aircraft Mishap," Tech. Rept., NASA Langley Research Center, Hampton, VA, 2004.
- [2] Peeters, B., and De Roeck, G., "Stochastic System Identification for Operational Modal Analysis: A Review," *Journal of Dynamic Systems, Measurement, and Control*, Vol. 123, No. 4, 2001, pp. 659–667. doi:10.1115/1.1410370
- [3] Nahom, T., Raveh, D. E., and Iovnovich, M., "Wind-Tunnel Study of the Autoregressive Moving-Average Flutter Prediction Method," *Journal of Aircraft*, Vol. 56, No. 4, July–Aug. 2019, pp. 1441–1454. doi:10.2514/1.C035203
- [4] Yagil, L., Raveh, D. E., and Idan, M., "Deformation Control of Highly Flexible Aircraft in Trimmed Flight and Gust Encounter," *Journal of Aircraft*, Vol. 55, No. 2, 2018, pp. 829–840. doi:10.2514/1.C034353
- [5] Reich, G. W., Raveh, D., and Zink, S., "Application of Active-Aeroelastic-Wing Technology to a Joined-Wing Sensorcraft," *Journal of Aircraft*, Vol. 41, No. 3, 2004, pp. 594–602. doi:10.2514/1.78
- [6] Davis, A., Chen, J. G., and Durand, F., "Image-Space Modal Bases for Plausible Manipulation of Objects in Video," *ACM Transactions on Graphics (TOG)*, Vol. 34, No. 6, 2015, pp. 1–7. doi:10.1145/2816795
- [7] Chen, J. G., Wadhwa, N., Cha, Y.-J., Durand, F., Freeman, W. T., and Buyukozturk, O., "Modal Identification of Simple Structures with High-Speed Video Using Motion Magnification," *Journal of Sound and Vibration*, Vol. 345, June 2015, pp. 58–71. doi:10.1016/j.jsv.2015.01.024
- [8] Wei, T., Zhongke, S., and Jie, C., "Aircraft Flutter Modal Parameter Identification Using a Numerically Robust Least-Squares Estimator in Frequency Domain," *Chinese Journal of Aeronautics*, Vol. 21, No. 6, 2008, pp. 550–558. doi:10.1016/S1000-9361(08)60173-9
- [9] Wnuk, V. P., Méndez, A., Ferguson, S., and Graver, T., "Process for Mounting and Packaging of Fiber Bragg Grating Strain Sensors for Use in Harsh Environment Applications," *Smart Structures and Materials*, International Soc. for Optics and Photonics, Bellingham, WA, 2005, pp. 46–53.
- [10] Krohn, D. A., and MacDougall, T. W., *Fiber-Optic Sensors: Fundamentals and Applications*, SPIE Press, Bellingham, WA, 2015.
- [11] Sante, R. D., "Fibre Optic Sensors for Structural Health Monitoring of Aircraft Composite Structures: Recent Advances and Applications," *Sensors*, Vol. 15, No. 8, 2015, pp. 18666–18713. doi:10.3390/s150818666
- [12] Kressel, I., Dorfman, B., Botsev, Y., Handelman, A., Balter, J., Pillai, A. C. R., Prasad, M., Gupta, N., Joseph, A. M., Sundaram, R., et al., "Flight Validation of an Embedded Structural Health Monitoring System for an Unmanned Aerial Vehicle," *Smart Materials and Structures*, Vol. 24, No. 7, 2015, Paper 075022. doi:10.1088/0964-1726/24/7/075022
- [13] Todd, M., Malsawma, L., Chang, C., and Johnson, G., "The Use of Fiber Bragg Grating Strain Sensors in Laboratory and Field Load Tests: Comparison to Conventional Resistive Strain Gages," Naval Research Lab. Tech. Rept. NRL/MR/5673-99-8418, Washington, D.C., 1999.
- [14] Ramakrishnan, M., Rajan, G., Semenova, Y., and Farrell, G., "Overview of Fiber Optic Sensor Technologies for Strain/Temperature Sensing Applications in Composite Materials," *Sensors*, Vol. 16, No. 1, 2016, p. 99. doi:10.3390/s16010099
- [15] Gherlone, M., Cerracchio, P., and Mattone, M., "Shape Sensing Methods: Review and Experimental Comparison on a Wing-Shaped Plate," *Progress in Aerospace Sciences*, Vol. 99, 2018, pp. 14–26. doi:10.1016/j.paerosci.2018.04.001
- [16] Ko, W. L., Richards, W. L., and Fleischer, V. T., "Applications of Ko Displacement Theory to the Deformed Shape Predictions of the Doubly-Tapered Ikhana Wing," Tech. Rept., NASA Dryden Flight Research Center, Edwards, CA, 2009.
- [17] Pak, C., "Wing Shape Sensing from Measured Strain," *AIAA Journal*, Vol. 54, No. 3, 2016, pp. 1068–1077. doi:10.2514/1.J053986
- [18] Pak, C.-G., and Truax, R., "Acceleration and Velocity Sensing from Measured Strain," *Novel Sensor Systems and Sensing Techniques*, AIAA Paper 2016-1229, 2016. doi:10.2514/6.2016-1229
- [19] Pak, C., "Unsteady Aerodynamic Force Sensing from Strain Data," *Journal of Aircraft*, Vol. 54, No. 4, 2017, pp. 1476–1485. doi:10.2514/1.C034140
- [20] Foss, G. C., and Haugse, E. D., "Using Modal Test Results to Develop Strain to Displacement Transformations," *Proceedings—SPIE The International Society for Optical Engineering*, SPIE International Soc. for Optical Engineering, Bellingham, WA, 1995, pp. 112–112.
- [21] Kang, L., Kim, D., and Han, J., "Estimation of Dynamic Structural Displacements Using Fiber Bragg Grating Strain Sensors," *Journal of Sound and Vibration*, Vol. 305, No. 3, 2007, pp. 534–542. doi:10.1016/j.jsv.2007.04.037
- [22] Jiang, H., van der Veeke, B., Kirk, D., and Gutierrez, H., "Real-Time Estimation of Time-Varying Bending Modes Using Fiber Bragg Grating Sensor Arrays," *AIAA Journal*, Vol. 51, No. 1, 2013, pp. 178–185. doi:10.2514/1.J051702
- [23] Skafte, A., Aenlle, M. L., and Brincker, R., "A General Procedure for Estimating Dynamic Displacements Using Strain Measurements and Operational Modal Analysis," *Smart Materials and Structures*, Vol. 25, No. 2, 2016, Paper 025020. doi:10.1088/0964-1726/25/2/025020
- [24] Suh, P., Chin, A., and Mavris, D., "Virtual Deformation Control of the X-56A Model with Simulated Fiber Optic Sensors," NASA TM-2014-216616, 2014.
- [25] Brincker, R., Skafte, A., López-Aenlle, M., Sestieri, A., D'Ambrogio, W., and Canteli, A., "A Local Correspondence Principle for Mode Shapes in Structural Dynamics," *Mechanical Systems and Signal*

- Processing*, Vol. 45, No. 1, 2014, pp. 91–104.  
doi:10.1016/j.ymsp.2013.10.025
- [26] Ramakrishnan, M., Rajan, G., Semenova, Y., and Farrell, G., “Overview of Fiber Optic Sensor Technologies for Strain/Temperature Sensing Applications in Composite Materials,” *Sensors*, Vol. 16, No. 99, 2016, pp. 1–27.
- [27] Othonos, A., and Kalli, K., *Fiber Bragg Gratings*, Artech House, Norwood, MA, 1999.
- [28] Rothhardt, M., Becker, M., Chojetzki, C., Linder, E., and Bartelt, H., “Fabrication and Applications of Draw Tower Gratings,” *Photonics and Fiber Technology*, OSA Technical Digest, 2016.  
doi:10.1364/BGPP.2016.BTh1B.1

C. Pettit  
Associate Editor